Charting the Landscape of Bardeen-Cooper-Schrieffer Superconductors in Experimentally Known Compounds

Marnik Bercx,[1,*] Samuel Poncé,[2,3,†] Yiming Zhang,[2] Giovanni Trezza,[4] Amir Ghorbani Ghezeljehmeidan,[5] Lorenzo Bastonero,[6] Junfeng Qiao,[7] Fabian O. von Rohr,[8] Giovanni Pizzi,[1] Eliodoro Chiavazzo,[4] and Nicola Marzari[1,6,7]

[1] *PSI Center for Scientific Computing, Theory, and Data, and National Centre for Computational Design and Discovery of Novel Materials (MARVEL), 5232 Villigen PSI, Switzerland*

[2] *European Theoretical Spectroscopy Facility, Institute of Condensed Matter and Nanosciences, Université catholique de Louvain, Chemin des Étoiles 8, B-1348 Louvain-la-Neuve, Belgium*

[3] *WEL Research Institute, Avenue Pasteur 6, 1300 Wavre, Belgium*

[4] *Department of Energy, Politecnico di Torino, 10129 Torino TO, Italy*

[5] *Electronic Components, Technology and Materials (ECTM), TU Delft, 2628 CD Delft, Netherlands*

[6] *Bremen Center for Computational Materials Science, and MAPEX Center for Materials and Processes, University of Bremen, 28359 Bremen, Germany*

[7] *Theory and Simulation of Materials (THEOS), and National Centre for Computational Design and Discovery of Novel Materials (MARVEL), École Polytechnique Fédérale de Lausanne (EPFL), 1015 Lausanne, Switzerland*

[8] *Department of Quantum Matter Physics, University of Geneva, 24 Quai Ernest-Ansermet, 1211 Geneva, Switzerland*

(Received 22 April 2025; revised 3 July 2025; accepted 1 August 2025; published 29 August 2025)

We perform a high-throughput computational search for novel phonon-mediated superconductors, starting from the Materials Cloud three-dimensional structure database of experimentally known inorganic stoichiometric compounds. We first compute the Allen-Dynes critical temperature (T_c^{AD}) for 4533 nonmagnetic metals using a direct and progressively finer sampling of the electron-phonon couplings. For the candidates with the largest T_c^{AD} value, we use automated Wannierizations and electron-phonon interpolations to obtain a high-quality data set for the most promising 250 dynamically stable structures, for which we calculate spectral functions, superconducting band gaps, and isotropic Migdal-Eliashberg critical temperatures. For 140 of these, we also provide anisotropic Migdal-Eliashberg superconducting gaps and critical temperatures. The approach is remarkably successful in finding known superconductors and we find 24 unknown ones with a predicted anisotropic T_c value above 10 K. Among them, we identify a possible double-gap superconductor (p-doped BaB_2), a nonmagnetic half-Heusler ZrRuSb, and the perovskite $TaRu_3C$, all exhibiting significant T_c values. Finally, we introduce a sensitivity analysis to estimate the robustness of the predictions.

DOI: 10.1103/sb28-fjc9

I. INTRODUCTION

Superconductors play an important role in many modern technologies, finding applications in magnetic-resonance-imaging machines, maglev trains, and large-scale research infrastructures such as the large-hadron collider at CERN. Over the past century, many classes of materials have been identified as new potential superconductors, but the most commonly used ones are still Nb-Ti alloys and A15 phases such as Nb_3Sn [1], which are well described by the Bardeen-Cooper-Schrieffer (BCS) theory of superconductivity [2,3]. High-temperature superconductors at ambient pressure, such as cuprates [4] and iron-based [5] superconductors, have much higher transition temperatures (T_c) but often come with challenges that hinder their practical use, such as brittleness, anisotropic superconductivity requiring precise grain alignment, and low critical currents, not to mention a still elusive theoretical foundation.

*Contact author: marnik.bercx@psi.ch
†Contact author: samuel.ponce@uclouvain.be

Until the last century, around one hundred stoichiometric ambient-pressure BCS superconductors had been found [6], representing only one (on average) new superconductor every year since the discovery of superconductivity, with most recent efforts delivering near-room-temperature critical temperatures, albeit at ultrahigh pressures [7]. Despite extensive efforts, targeted or serendipitous discoveries have not fulfilled the demand for high-performance superconductors for industrial and scientific applications and a cost-effective computational search is also desirable.

During the past few decades, first-principles calculations have played an increasingly important role in both understanding and predicting the material-specific aspects of superconductivity (for a review, see, e.g., Ref. [2]). Although understanding high-temperature superconductivity is still challenging [8], conventional BCS superconductors are typically tractable and can be studied readily via well-established techniques [9–11]. Therefore, a number of efforts have recently emerged to find new phonon-driven superconductors using *ab initio* evolutionary search [12,13], machine-learning approaches [14–22] or high-throughput screening [16,23–26]. Machine-learning approaches are often (but not exclusively [27]) based on training on the experimental SuperCon database [6,20], which contains chemical formulas but not the crystal structures and focuses primarily on nonconventional superconductors. Instead, high-throughput studies based on first-principles calculations have relied on coarse momentum-grid integrations for screening and have performed accurate calculations on a small number of promising candidates. As shown before [28] and also highlighted here, a precise calculation of the electron-phonon interactions, essential for determining superconductivity, typically requires an ultradense sampling of the Brillouin zone.

The EPW code [29,30] can perform such precise interpolations of the electron-phonon matrix elements at a low computational cost. However, performing an extensive search using these advanced methods has remained elusive up to now, as obtaining the relevant maximally localized Wannier functions (MLWFs) [31] has historically required a combination of chemical intuition and trial-and-error efforts. In this work, we combine recent developments in automated Wannierization algorithms [32] with the AiiDA computational infrastructure [33,34] to perform a systematic and reproducible screening of the Materials Cloud three-dimensional (3D) database (MC3D) [35] for BCS superconductors. Importantly, the MC3D has been obtained combining three crystal-structure databases (the Crystallography Open Database (COD) [36], the Inorganic Crystal Structure Database (ICSD) [37], and the Materials Platform for Data Science (MPDS) [38]), filtering out, to the maximum extent, entries that are not backed by experimental results, and keeping only stoichiometric compounds at standard conditions. The goal here is to explore, with state-of-the-art electronic structure calculations, known materials for novel properties, in the same spirit as Mounet *et al.* [39], rather than predicting novel materials (with all the challenges that it entails for novel properties [40]). Starting from a set of 4533 nonmagnetic metals (as predicted from Kohn-Sham density-functional theory (DFT), which under-estimates band gaps), we first perform an initial screening at progressively higher levels of precision using the Standard Solid-State Pseudopotentials (SSSP) library [41] which also includes projector-augmented-wave-method [42] pseudopotentials. Based on these results, we select the top 949 materials, for which we perform a new structural relaxation but this time using the PseudoDojo library [43] which contains exclusively norm-conserving pseudopotentials. Out of these, we exclude 47 materials found to be magnetic after an additional test, 347 materials due to calculation failures or unconverged results, 270 showing unstable phonon modes, and 33 due to an insufficient quality in the interpolated band structures. From the remaining 252 promising candidates, we compute Wannier functions, Eliashberg spectral functions $\alpha^2F(\omega)$, and the isotropic Migdal-Eliashberg superconducting T_c^{iso}. At that stage, two fail due to node failure, giving 250 T_c^{iso}. Finally, for the 144 materials with a T_c^{iso} larger than 5 K, we perform a full anisotropic Migdal-Eliashberg superconducting calculation. These final calculations are memory intensive and four fail for this reason, leaving a final set of 140 anisotropic T_c^{aniso}-value predictions. For each material, our database, openly available on the Materials Cloud archive [44] and presented in the Supplemental Material [45], reports electronic band structures and phonon dispersions, Eliashberg spectral functions $\alpha^2F(\omega)$, Allen-Dynes T_c values [46], and isotropic and anisotropic Migdal-Eliashberg superconducting gaps $\Delta_{n\mathbf{k}}$ and T_c values [28]. To our knowledge, this effort represents the largest database of converged anisotropic superconducting Migdal-Eliashberg calculations.

From the list of 250 T_c^{iso} candidates, we find that 82 of them are known superconductors with a T_c value in reasonable agreement with experiment when accounting for the experimental mismatch with the computed structure. The remaining 168 compounds are not known to be superconducting and 24 of these have a predicted T_c value above 10 K. To ensure the robustness of these predictions with respect to the (approximate) Kohn-Sham band structures and the position of the Fermi energy (which in experiments can be affected by defects and unintentional doping or self-doping), we introduce a sensitivity criterion based on homogeneous doping within the rigid-band approximation. We then discuss in detail three appealing examples: the hole-doped two-gap superconductor BaB_2, the potentially first half-Heusler superconductor ZrRuSb, and the perovskite $TaRu_3C$.

II. RESULTS

A. Screening of the MC3D database and high-throughput calculations

We start our screening from a set of Crystallographic Information File (CIF) files extracted from three databases available in the literature: MPDS [38], ICSD [37], and COD [36]. We have analyzed these extensively and combined them into a database of unique experimentally known structures at ambient conditions. Subsequently, each structure has been optimized with DFT calculations following a strict protocol, after initializing them in a high-spin ferromagnetic state to identify magnetic materials. The optimized geometries are published as the Materials Cloud 3D database (MC3D) [35], details of which are provided in Sec. 1 of the Supplemental Material [45]. Starting from the MC3D, nonmagnetic materials with 12 atoms or less in the primitive unit cell are considered (see Fig. 1). Finally, metals are selected based on the Fermi level and occupations at the Kohn-Sham DFT level, leading to 4533 compounds that we screen for potential superconductivity.

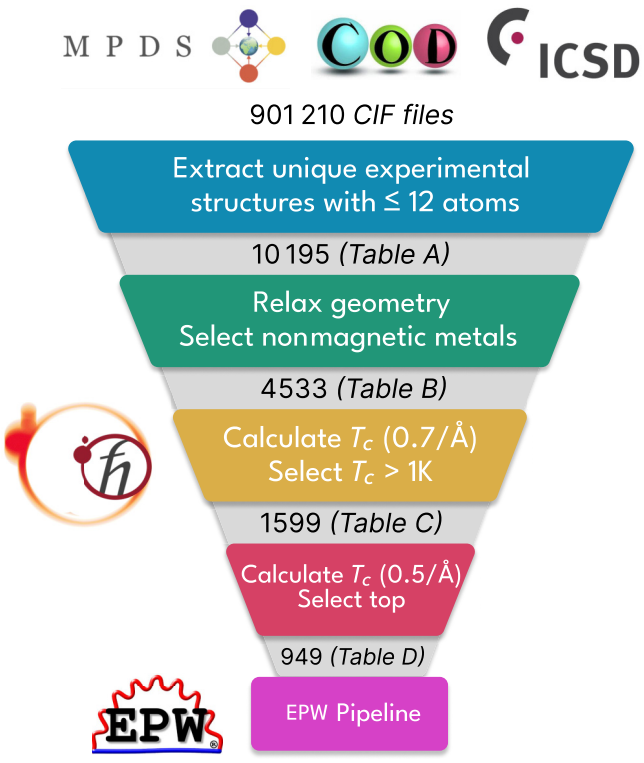

FIG. 1. The initial screening of the experimentally known materials. The structures are extracted from the MPDS [38], COD [36], and ICSD [37] databases using the QUANTUM ESPRESSO electron-phonon coupling workflow. Tables A, B, C, and D correspond to the full list of materials belonging to each category and published with this work [44].

Next, we calculate the electron-phonon interactions using density-functional perturbation theory as implemented in the QUANTUM ESPRESSO distribution [47]. In our initial screening, we have created a workflow to calculate the Eliashberg spectral function and corresponding Allen-Dynes T_c^{AD}, progressively increasing the precision of the calculations by using denser and denser phonon (**q**) and commensurate electron (**k**) sampling grids. In the first step, we use a coarse homogeneous **q**-point grid with density 0.7 $\mathrm{Å}^{-1}$ and identify structures with a T_c^{AD} above 1 K as potential superconductors. In the second iteration, a **q**-point grid with density 0.5 $\mathrm{Å}^{-1}$ is used, from which we make a selection of the 949 structures with the highest T_c value: see Sec. IV for additional details on the workflow and Sec. 2 of the Supplemental Material [45] for details on the structures, soft modes, and failure rate. Although this initial screening, based on the linear-interpolation approach of Wierzbowska *et al.* [48], is a solid first step to detect materials as superconductors, a significant number of structures have a T_c^{AD} that is not yet converged with respect to sampling (see Sec. 2 of the Supplemental Material [45]). Since denser grids are computationally prohibitive and the Allen-Dynes approximation to the T_c value has limited accuracy [28], in the final step of our screening we use the EPW code [29,30] to interpolate electron-phonon matrix elements on ultradense grids at low computational cost. Thus, we take the top 949 candidates with the goal of first calculating the isotropic Eliashberg T_c value using the EPW code (see Fig. 2). Since magnetism aligns spins in a particular direction, it breaks the spin-singlet pairing of Cooper pairs [49] and is detrimental to standard superconductivity. We therefore first perform both a nonmagnetic and ferromagnetic structural relaxation of all the materials to determine if the ferromagnetic solution is more stable (in order to discard it), resulting in a set of 893 nonmagnetic metals. To perform the interpolations with EPW, we rely on the **k**-point version of the "selected columns of the density matrix" method (SCDM-*k*) [32] to automatically generate maximally localized Wannier functions that span the occupied and lowest unoccupied bands, and that act as an essentially exact interpolator of the Kohn-Sham band structures [31]. In the coarse-grid calculations required to set up the Wannier interpolations, the workflows for 275 compounds failed, mostly due to issues related to reaching computational convergence or resource limits (out-of-memory errors or time limits) (for a detailed account of the error rates, see Sec. 2 of the Supplemental Material [45]). For the remaining 618 coarse-grid calculations, we interpolate the phonon band structure and apply an acoustic sum rule that enforces the 15 Born-Huang conditions [50] and then check the dynamical stability of the structure.

At this stage, we exclude six materials due to non-Hermiticity of the dynamical matrices due to the dipole-dipole interatomic force constant ansatz [51]; for the 612

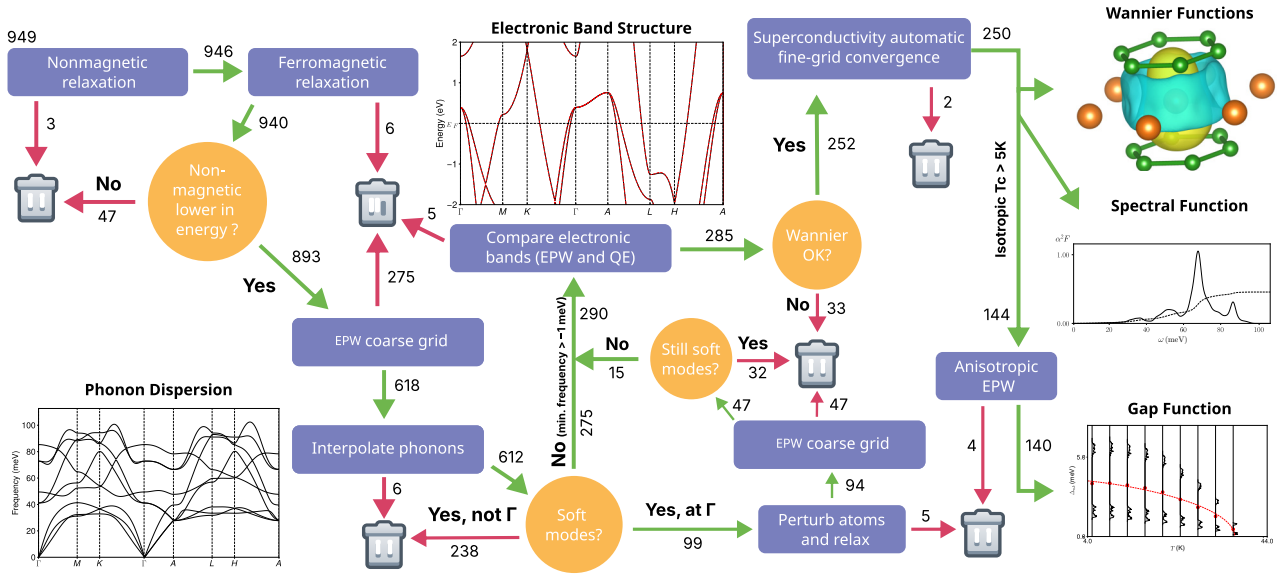

FIG. 2. The flowchart of the electron-phonon Wannier (EPW) workflow. The pipeline starts from the top candidates obtained from the initial QUANTUM ESPRESSO screening. The red arrows corresponds to structures that are discarded along the pipeline due to failed runs, magnetism, the presence of soft modes, or an insufficient quality of the Wannierization.

interpolated phonon dispersions, we find that 238 have soft modes away from Γ, which indicates potential instabilities. We also find 99 structures with soft modes at Γ that we try to stabilize by applying a random perturbation of the atomic positions and relaxing the geometries; this allows us to stabilize a further 15 structures. For the remaining 290 materials, we assess the quality of the Wannier-function interpolation by comparing an electronic band structure directly calculated with DFT and the interpolated one, accepting a maximum 50-meV-weighted band distance [41]. This leads us to 252 structures that are dynamically stable and have accurate Wannier interpolations of the electronic band structure. These are then passed to the superconductivity workflow (see Fig. 2), which performs an automatic convergence of the interpolation mesh based on T_c^{AD}. Once T_c^{AD} is found to converge within 1 K, another run is performed to calculate the isotropic Eliashberg critical temperature T_c^{iso} with the corresponding interpolation mesh. During this automatic convergence of the interpolated momentum meshes, we exclude two materials due to convergence issues, which leaves 250 materials for which we perform a converged T_c^{iso} calculation. For the 144 structures that have a T_c^{iso} above 5 K, we perform a final anisotropic Eliashberg T_c^{aniso} calculation to obtain the superconducting gap $\Delta_{n\mathbf{k}}(T)$ on the Fermi surface. During the anisotropic Eliashberg calculations, four materials failed due to out-of-memory error or reaching execution time limits, leading to a final set of 140 high-quality tightly converged anisotropic Eliashberg results. Additional details on the EPW workflow are provided in Sec. IV.

B. Analysis of the supercond-EPW database

The resulting database of structures and properties, called *supercond*-EPW, contains the primitive unit cells, electronic band structures, phonon dispersions, Eliashberg spectral functions $\alpha^2F(\omega)$, $T_c^{\mathrm{AD},f}$ on the fine grid, and T_c^{iso} for 250 metals. For 140 of these having a $T_c^{\mathrm{iso}} > 5$ K, we also provide the T_c^{aniso} and $\Delta_{n\mathbf{k}}(T)$ values. These results are reported in Sec. 7 of the Supplemental Material [45] and on the Materials Cloud archive [44]. To understand which of the structures among these candidates are known superconductors, we perform an extensive literature survey and search for reported critical temperatures. We find that 137 out of 250 materials have been experimentally investigated for their critical temperature and, for 82 of them where the structure and not only the chemical formula is reported, we can confirm that the experimental structure matches the calculated one (see Sec. 7 of the Supplemental Material [45]). From these, eight are false positives (not superconducting down to 1 K). This means that 74 (90%) of the structures for which we have a confirmed experimental result are true positives, which is a strong indication that our procedure can reliably identify superconducting materials from a large pool of initial candidates. To assess the risk of removing materials erroneously (false negatives), we have extracted a list of 32 well-known superconductors from the literature and investigated how many of these are discarded by our procedure (see Sec. 3 of the Supplemental Material [45]). Of these, we missed seven; these include three failures in the phonon calculation (which could be resolved in future improvements of the workflows to make

them more robust) and two due to an insufficient interpolation quality of the band structure (an issue that can be resolved via improved approaches to automated Wannierization using projectability disentanglement [52]). Finally, we find that the remaining two cases are due to the presence of soft modes in the phonon dispersions. We highlight the particular case of δ-NbN with an experimental T_c value of 16 K [53], which was discarded due to soft modes at the $\mathbf{q} = \mathbf{X}$ point, the reason being that the experimental δ-NbN can only be prepared with a small N deficiency and that it has been found that the disorder can be simulated with a large electronic smearing [54].

In Table I, we list the top 30 compounds for which we have an experimental result and a matching structure, with the highest T_c^{iso}, along with the corresponding T_c^{AD} temperatures for the coarse and fine grids, T_c^{aniso} and the reported experimental value. In the list, several classes of well-known superconductors are present, such as elemental Nb and Tc, MgB_2, and the A15 phases (Nb_3Sn and Mo_3Os). However, we also note some of the false positives mentioned above, RuO_2 and TaB_2, which have a high calculated T_c value, yet experimental reports indicate that they are not superconducting. Moreover, in some cases we find a large discrepancy between the reported experimental critical temperature and the calculated ones. These results indicate that comparing computational predictions with experimental data presents certain challenges. These include (i) the limited availability of comprehensive databases, (ii) uncertainties in the structures present in experiments, and (iii) the presence of material complexities such as doping, grain boundaries, defects, strain, off-stoichiometries, or site-antisite mixing, all of which can influence the T_c value and may not be captured by state-of-the-art computational methods. On the computational side, the most significant approximations are (i) the neglect of spin fluctuation [55] in our calculations, (ii) the use of a fixed Coulomb parameter $\mu^* = 0.13$, and (iii) the use of Kohn-Sham band structure; DFT is not a spectral theory, and more expensive many-body perturbation theory should be employed to calculate electronic excitations [56]. Removing experimental data with reported limitations and materials where spin fluctuation is known to dominate, we find that our calculated T_c values are in reasonable agreement with the experimental data (for detailed reports and comparisons, see Sec. 3 of the Supplemental Material [45]).

In Table II, we report the top 30 experimentally known compounds that are predicted by the workflows discussed here to be BCS superconductors. We note that VC, CrH, and Be_2B have also been reported as superconductors in the computation work of Choudhary *et al.* [16], with predicted T_c values of 28.1, 10.7, and 8.8 K, respectively. These values are in good agreement with the 20.7, 13.4, and 10.9 K isotropic T_c values that we have computed. In addition, the W_2N_3 monolayer [94] and $TaMo_2B_2$ [95] have also been proposed theoretically, with predicted T_c values of 21 and 12 K, respectively. The other materials presented in Table II are novel in the sense that they have never been reported as superconductors. However, many materials in the list contain heavy elements with partially occupied d or f shells and could be magnetic, even if the initial screening found them to be nonmagnetic. Henceforth, we additionally validate all transition-metal

TABLE I. The top 30 compounds that are known superconductors. From the screening, the list is ordered according to the computed T_c^{aniso}, together with chemical formulas, space-group (SG) number, Allen-Dynes transition temperature ($T_c^{\mathrm{AD},c}$ in kelvin) computed with direct coarse grids, Allen-Dynes transition temperature ($T_c^{\mathrm{AD},f}$ in kelvin) interpolated on fine grids, isotropic Eliashberg transition temperature (T_c^{iso}) in kelvin, anisotropic Eliashberg transition temperature (T_c^{aniso}) in kelvin, and the experimental T_c value. The electron-phonon coupling strength λ and logarithmic phonon frequency $\omega_{\log}$ entering the Allen-Dynes formula are reported in Sec. 7 of the Supplemental Material [45]. All the predicted T_c values have been obtained with an effective Coulomb potential of $\mu^* = 0.13$, a reasonable assumption for many experimentally verified superconductors. All experimental references and full details of the structures and properties are provided in Sec. 7 of the Supplemental Material [45].

Material	SG	$T_c^{\mathrm{AD},c}$	$T_c^{\mathrm{AD},f}$	T_c^{iso}	T_c^{aniso}	Experimental T_c
MgB_2	191	25.6	12.3	16.5	36.8	39.0 [57]
MoN	187	23.7	26.7	32.1	36.6	4.0–6.0 [58]
Nb_3Sn	223	11.8	18.3	25.6	35.6	17.9–18.3 [59,60]
RuO_2	136	11.9	21.9	26.1	34.0	<0.3 [61]
PdH	225	30.0	21.2	25.9	30.1	8.5–11.0 [62,63]
$TaSe_2$	194	4.1	8.9	20.1	27.5	0.1 [64]
$NbSe_2$	194	5.8	16.3	21.9	26.7	5.7 [65]
V	229	19.0	20.4	27.1	26.1	4.7–5.4 [66,67]
MoC	194	22.3	17.3	20.8	25.5	8.0 [68]
V_3Pt	223	10.2	14.9	18.5	25.2	3.0 [69]
VC	225	18.9	17.2	20.7	25.0	1.8 [70]
NbS_2	194	8.5	18.5	24.3	25.0	6.1 [71]
TaS_2-2H	194	4.7	16.2	21.3	23.7	0.5–2.2 [72,73]
TaB_2	191	14.4	15.5	17.5	21.6	<1.5 [74]
Ta_3Sn	223	9.4	11.4	15.6	21.5	4.2–8.35 [75,76]
Nb	229	13.1	15.1	19.7	21.2	9.1–9.5 [77,78]
Mo_3Os	223	16.3	15.4	18.9	20.8	7.3–12.7 [79,80]
CaC_6	166	10.5	11.6	12.1	19.1	11.5 [81]
ZrN	225	10.3	9.8	12.6	18.6	9.3–9.6 [82]
ZrRuP	189	8.2	13.0	15.9	17.9	13.3 [83]
YCI	12	4.9	8.5	13.6	17.7	9.85 [84]
Ni_3ZnN	221	8.4	14.5	18.3	17.6	3.0 [85]
Tc	194	11.9	12.7	16.3	17.1	7.9–11.2 [78,86]
YCCl	12	3.9	8.0	12.0	14.9	2.3 [84]
TiN	225	10.3	9.9	12.9	14.2	5.5–5.6 [82,87]
NbB_2	191	9.0	10.6	13.0	13.8	0–5.0 [88,89]
HfN	225	10.4	9.7	11.7	13.7	5.8 [90]
$BaGe_3$	194	2.5	8.7	10.9	13.2	4.0–6.5 [91,92]
ScSe	225	5.0	8.0	10.0	12.3	3.7 [93]
Sn	139	4.9	7.7	11.0	11.6	3.7 [78]

TABLE II. The top 30 compounds from this screening that are predicted to be BCS superconductors. The largest T_c (K) values for materials predicted to be BCS superconductors, following the same convention as Table 1. For $T_c^{\mathrm{AD},f}$ and T_c^{iso}, we provide a sensitivity analysis that gives the change of T_c upon homogeneous electron (superscript) and hole (subscript) doping of 10^{21} cm^{-3}. Materials that have a potentially magnetic ground state based on self-consistent Hubbard calculations [99], or for which we could not confirm the structure or source, are noted. BaB_2 is listed separately, as a hole doping of 0.065 holes per unit cell is required to stabilize the phase.

Material	SG	$T_c^{\mathrm{AD},c}$	$T_c^{\mathrm{AD},f}$	T_c^{iso}	T_c^{aniso}
W_2N_3	194	11.3	$20.2^{+0.6}_{-0.9}$	$26.3^{+0.6}_{-1.0}$	33.7
Be_2B	225	9.7	$7.7^{+0.5}_{-0.3}$	$10.9^{+0.7}_{+0.2}$	22.1
PtO	131	8.9	$13.3^{+0.1}_{-0.1}$	$16.3^{+0.3}_{-0.2}$	19.0
Mo_3Be	223	9.3	$8.1^{+0.4}_{-0.4}$	$10.5^{+0.4}_{-0.4}$	17.6
AsTe	225	6.4	$10.6^{+0.5}_{-0.4}$	$13.8^{+0.6}_{-0.6}$	17.2
TaCoSb	216	11.4	$11.4^{-0.7}_{-2.7}$	$14.1^{-0.7}_{-3.6}$	16.8
TaS	187	8.4	$9.3^{-0.8}_{+0.0}$	$11.3^{-1.0}_{-0.6}$	13.6
ZrRuSb	216	5.1	$8.9^{+0.5}_{-0.7}$	$9.9^{+0.5}_{-0.9}$	13.2
YIr_3B_2	12	6.2	$4.8^{-0.2}_{+0.2}$	$8.6^{-0.3}_{+0.3}$	12.2
Zr_2Al	140	3.0	$5.7^{+0.2}_{-0.2}$	$7.4^{+0.4}_{-0.0}$	7.8
MoB	63	3.9	$4.8^{-0.1}_{-0.1}$	$6.8^{-0.1}_{-0.1}$	7.7
HfRuSb	216	3.8	$4.9^{+0.5}_{-0.5}$	$6.6^{+0.6}_{-0.6}$	6.4
Potentially magnetic					
$TaRu_3C$	221	15.0	$16.5^{-1.9}_{+1.4}$	$21.0^{-2.6}_{+4.4}$	25.0
$NbRu_3C$	221	15.6	$17.5^{-1.5}_{+1.2}$	$21.8^{-2.0}_{+1.7}$	24.9
NbCoSb	216	12.4	$16.3^{-1.5}_{+1.0}$	$20.4^{-1.7}_{+1.4}$	21.4
IrS_2	205	12.6	$13.2^{-0.3}_{-0.0}$	$16.1^{-0.3}_{-0.0}$	20.8
ZrS	129	10.9	$10.7^{+0.0}_{-0.1}$	$13.4^{-0.3}_{-0.2}$	18.8
Ti_3SnH	221	7.9	$11.7^{-1.4}_{-0.3}$	$14.6^{-2.8}_{-1.4}$	18.7
RhS_2	205	16.6	$9.4^{-0.6}_{+1.0}$	$11.8^{+0.5}_{+0.7}$	17.3
CrH	225	9.8	$10.6^{-0.2}_{+0.3}$	$13.4^{-0.2}_{+0.3}$	16.9
TiRuSb	216	7.5	$10.1^{+0.7}_{-1.0}$	$12.9^{+1.1}_{-1.9}$	13.6
RhSe	194	7.7	$8.3^{-1.1}_{+1.0}$	$10.8^{-1.6}_{+0.8}$	11.9
Ti_2Ga	194	3.9	$5.2^{+0.1}_{-0.2}$	$7.1^{-0.1}_{-0.4}$	8.3
Unconfirmed source					
YC	225	15.4	$13.4^{+0.7}_{-0.9}$	$17.1^{+1.0}_{-0.9}$	22.0
$TaMo_2B_2$	127	9.5	$9.7^{-0.7}_{+0.6}$	$12.1^{-0.8}_{+0.5}$	14.3
Zr_3Sn	223	8.8	$7.7^{-0.3}_{+0.3}$	$9.9^{-0.3}_{+0.2}$	14.2
$LiAl_2Ge$	225	3.8	$8.0^{+0.1}_{-0.0}$	$9.7^{+0.1}_{-0.1}$	10.8
Li_2AlGe	216	6.2	$5.8^{+0.3}_{-0.2}$	$7.3^{+0.3}_{-0.2}$	9.3
AgF_2	14	8.1	$5.1^{-0.7}_{+1.0}$	$6.7^{-1.4}_{+0.5}$	7.5
Hole-doped stabilization					
BaB_2	191	20.4	$21.4^{+0.2}_{-0.1}$	$33.0^{+0.3}_{-0.2}$	61.6

compounds in Table II employing state-of-the-art self-consistent relaxations using on-site and intersite Hubbard correction [96] for the materials in their nonmagnetic and ferromagnetic configurations, using the HP code [97,98] to determine U and V from first principles. The Hubbard-corrected band structure of the materials and their magnetic energy landscape are reported in Sec. 4 of the Supplemental Material [45] and the materials with a ferromagnetic ground state are noted in Table II. Since magnetism is detrimental to BCS superconductivity [49], all results are reported for materials in their PBE nonmagnetic ground state.

Overall, the material with the highest predicted T_c^{aniso} value is BaB_2, which displays interesting two-gap superconductivity, reminiscent of the well-known behavior observed in isostructural and isoelectronic MgB_2 [57]. One could wonder how such a simple binary material had not been discovered already. As discussed in the next section, we find that pristine BaB_2 displays a small instability and relaxes to a different structure than the experimentally reported one. However, upon p doping of 0.065 holes per unit cell, the MgB_2-like phase stabilizes and shows high promise. Despite these results, careful consideration is necessary, since the DFT electronic band structure and Fermi-level position are inexact [100]. We therefore introduce a sensitivity analysis for the predictions, which consists in computing the change of the Allen-Dynes T_c value and the isotropic T_c value upon a homogeneous electron (+) and hole (−) doping of 10^{21} cm^{-3}. This doping corresponds to a medium-to-high metallic doping that can realistically be achieved through substitution or interstitial doping (through ion implantation, the Fermi level can be experimentally fine tuned at the millielectronvolt level to achieve the optimal doping to enhance the superconducting critical temperature [101]). Doping levels above 10^{22} cm^{-3} are usually not feasible due to potential phase segregation [102]. We translate the doping density into energy shifts around the Fermi level, where changes of T_c can be evaluated via the Eliashberg equations (for a detailed description, see Sec. 5 of the Supplemental Material [45]). We report this sensitivity analysis in Table II and find 13 superconductors for which the T_c value changes by less than 0.5 K upon $\pm 10^{21}$ cm^{-3} doping and thus can be considered more robust with respect to the predictions.

An interesting class of structures in Table II are the half-Heusler compounds NbCoSb, TaCoSb, TiRuSb, ZrRuSb, and HfRuSb [103]. Many properties of Heusler compounds [104], including the electronic structure, are typically related to their valence electron count (VEC). The half-Heusler is one of the most common structure types for ternary intermetallics and half-Heusler phases commonly have a VEC of 18 per formula unit, corresponding to a closed-shell configuration. Therefore, half-Heusler phases are typically semiconducting, whereas the few open-shell half-Heusler phases are typically metallic in nature [105]. Although many examples of full-Heusler superconductors have been discussed in the literature, both in experimental [106] and computational [107] work, superconductivity in half-Heuslers is found to be nonconventional [108,109] or topological in nature [110] and related to their noncentrosymmetric structure [111]. For full-Heusler phases, Graf *et al.* [106] have proposed a relationship between the VEC and superconducting properties, citing a prevalence of superconducting full Heuslers with VEC 27.

For TiRuSb, HfRuSb, and ZrRuSb, the VEC is 17, and for NbCoSb and TaCoSb the VEC is 19, indicating an electron deficiency and surplus compared to VEC 18, respectively. Reports on conventional superconductivity in half-Heusler compounds are scarce, making this an exciting avenue for further exploration. There are also several perovskite structures in the list, including $TaRu_3C$, Ni_3ZnN, $NbRu_3C$, Ti_3TlN, and Ti_3SnH, where $TaRu_3C$ has the highest predicted T_c^{aniso} value, of 25.0 K. Perovskites [112] and antiperovskites [113] are well-known families of superconductors where empirical relations exist between T_c and cation charges in the perovskite cages [114].

C. Analysis of BaB_2, ZrSbRu, and $TaRu_3C$

In this section, we focus specifically on BaB_2, the ZrRuSb half-Heusler, and $TaRu_3C$, as these constitute interesting candidates. For these three materials, we have performed more detailed calculations using the intermediate representation (IR) [11] of the Migdal-Eliashberg implementation in the EPW software. In Figs. 3 and 4, we show their electronic and vibrational properties, spectral function, isotropic and anisotropic superconducting-gap function $\Delta_0(i\pi T)$ value, and $\Delta_{n\mathbf{k}}(i\pi T)$ value. For the anisotropic gap function, we show the histogram of the superconducting-gap function $\rho(\Delta)$ at the lowest Matsubara frequency $\Delta_{n\mathbf{k}}(i\pi T)$, defined as [11]

$$\rho(\Delta(T)) = \sum_{n\mathbf{k}} \delta(\Delta_{n\mathbf{k}}(i\pi T) - \Delta(T))\delta(\epsilon_{n\mathbf{k}} - \epsilon_F), \quad (1)$$

where ϵ_F is the Fermi level. The temperature-dependent isotropic gap $\Delta_0(T)$ and anisotropic gap $\Delta_{n\mathbf{k}}(i\pi T)$ are fitted by the BCS-type gap function $\Delta^{\text{BCS}}(T) = \Delta^{\text{BCS}}(0)\sqrt{1-(T/T_c)^{\beta}}$. To further analyze the structure of the electron-phonon coupling, we compute the mode-resolved and band-resolved coupling constants $\lambda_{\mathbf{q}\nu}$ and $\lambda_{n\mathbf{k}}$.

We start with a closer investigation of BaB_2, which is an isostructural and isoelectronic counterpart of the well-known two-gap superconductor MgB_2 that was experimentally discovered more than two decades ago [57].

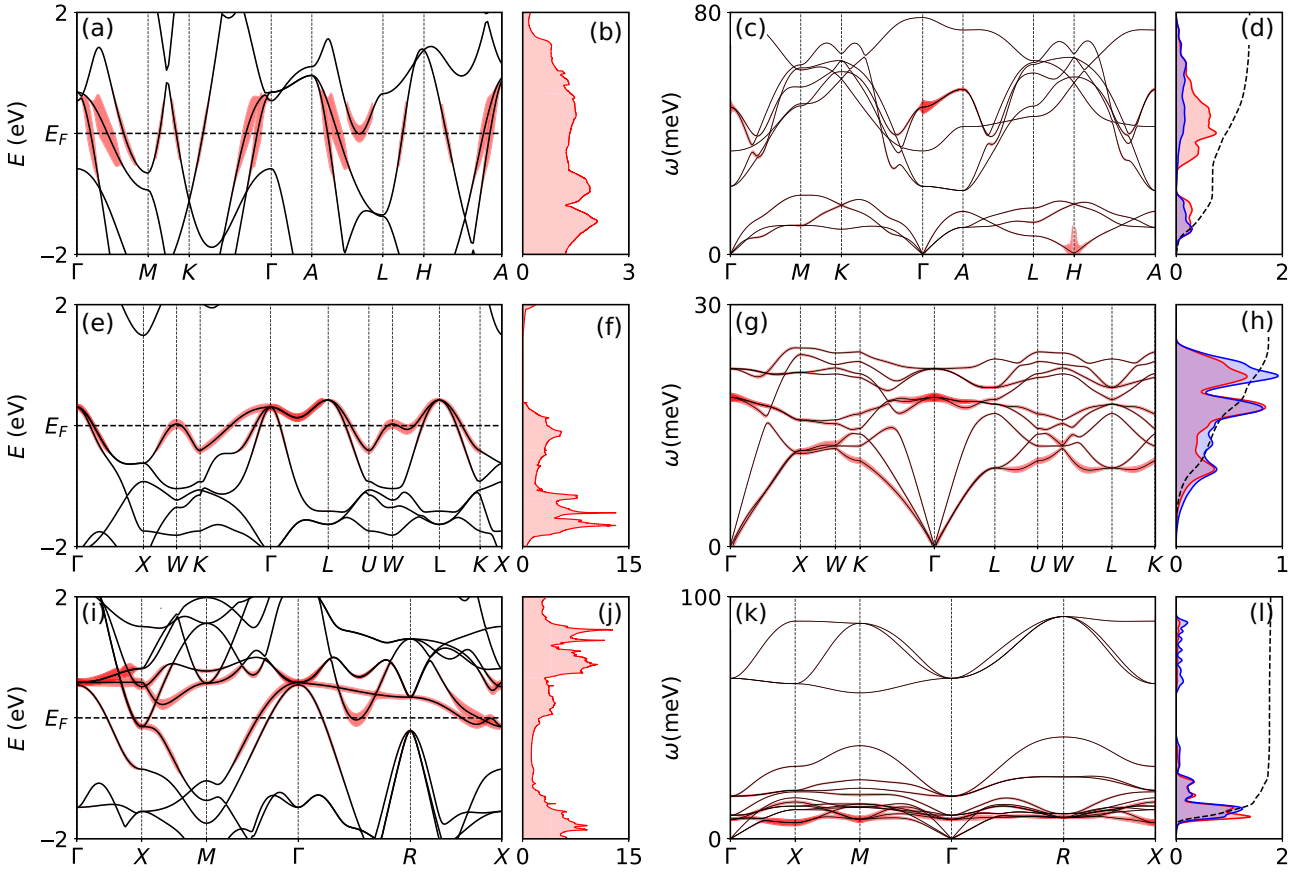

FIG. 3. Analysis of the electronic, vibrational, and electron-phonon properties of BaB_2, ZrSbRu, and $TaRu_3C$. The electron band structures, electron density of states, phonon dispersions, spectral functions (red), accumulated spectral functions (dashed black), and phonon density of states (blue) for (a)–(d) doped BaB_2, (e)–(h) ZrRuSb, and (i)–(l) $TaRu_3C$. The band-resolved electron-phonon coupling constant $\lambda_{n\mathbf{k}}$ and the mode-resolved electron-phonon coupling constant $\lambda_{\mathbf{q}\nu}$ are plotted on the band structures and phonon dispersion as proportional to the linewidth. The largest band-resolved coupling constants are 2.82, 1.11, and 3.16, respectively.

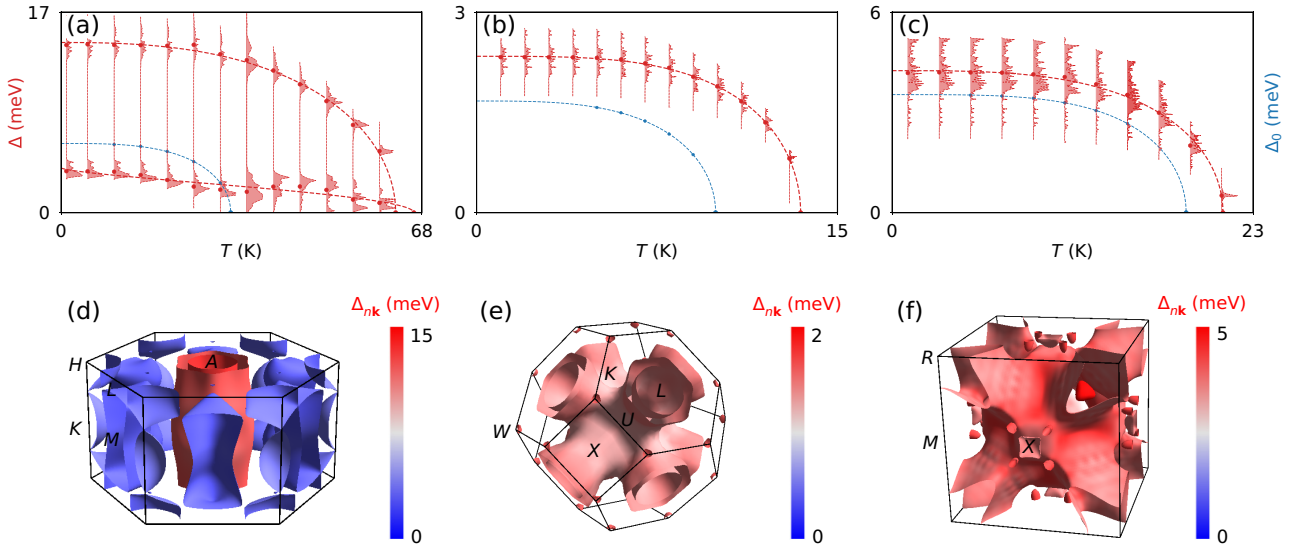

FIG. 4. Analysis of the superconducting properties of BaB_2, ZrSbRu, and $TaRu_3C$. The isotropic gap functions Δ_0 (blue), histograms of the anisotropic gap functions $\rho(\Delta, T)$ (red), and superconducting gaps on Fermi surfaces for (a),(d) doped BaB_2 (10 K), (b),(e) ZrRuSb (5 K), and (c),(f) $TaRu_3C$ (5 K).

Although BaB_2 has been investigated in the context of superconductivity [115], its critical temperature has never been determined or predicted. Based on the results from our high-precision workflow described in Fig. 2, the pristine hexagonal phase is unstable due to a soft mode at the H point. Upon further investigation, we find that homogeneous hole doping above 0.065 per unit cell (1.46×10^{21} cm^{-3}) can stabilize the pristine phase while superconductivity remains unaffected up to at least 0.1 per unit cell (see Sec. 6 of the Supplemental Material [45]). Analogously to MgB_2, BaB_2 is a strongly coupled material with $\lambda = 1.39$. From Figs. 3(a)–3(d), one can see that the electron-phonon coupling is highly anisotropic, with a dominant optical phonon mode at Γ and an acoustic mode at H, which is unstable in the undoped structure. The interpolated isotropic transition temperature is $T_c^{\mathrm{iso}} = 32.0$ K, larger than the $T_c^{\mathrm{AD}} = 24.4$ K. According to Figs. 4(a) and 4(d), the Fermi surfaces are composed of two nested cylinders along the Γ-A line, with a superconducting gap of 11.54 meV and pockets centered at H, M, and K points with a superconducting gap of 1.50 meV. This corresponds to two anisotropic critical temperatures $T_c^{\mathrm{aniso},1} = 61.6$ K and $T_c^{\mathrm{aniso},2} = 60.6$ K, larger than the isotropic approximation due to the strong anisotropy. In Fig. 3(a), the band-resolved coupling strength also shows that the coupling is dominated by the two nested cylindrical Fermi-surface sheets.

We continue with the five half-Heusler phases NbCoSb, TaCoSb, HfRuSb, TiRuSb, and ZrRuSb, studying their magnetic states in more detail. The magnetic landscape is probed using a random forest search where magnetic configurations are constrained and then relaxed using electronic structure calculations at the PBE and PBE+U level with the ROMEO code [116]. The magnetic search is performed in the conventional supercell (12 atoms) to allow for more complex magnetic states. The algorithm is stopped when the ratio of newly discovered unique states to the number of trials goes below 0.2. We show the magnetic energy landscape for each configuration for the four half-Heuslers in Sec. 4 of the Supplemental Material [45] and find that all are nonmagnetic at the PBE level and that ZrRuSb is the only one that also remains nonmagnetic at the PBE+U level. We therefore investigate ZrRuSb further and find that its Fermi surface is composed of a sphere centered at Γ [invisible in Fig. 4(e)], two nested connected necklike formations at the L points, and small spheres centered at the W points. According to Figs. 3(e), 3(g) and 3(h), the electron-phonon coupling is isotropic overall, dominated by the phonon density of states, through enhancement of the optical Γ phonon and acoustic phonons near X and L. The interpolated isotropic and anisotropic transition temperatures are 9.9 and 11.1 K, respectively. However, we note in the density of states of Fig. 3(f) that the high predicted superconductivity in ZrRuSb comes from the position of the Fermi level being located near a van Hove singularity, with a flat band around the W **k**-point. This means that this prediction might not be robust upon small changes of the Fermi level resulting from DFT inaccuracies or experimental conditions. This is supported by the sensitivity check shown in Table II, where ZrRuSb varies by over 1 K upon a medium doping level. Finally, we study the perovskite $TaRu_3C$ as our highest-T_c (potentially magnetic) material from Table II. Indeed, all these materials are nonmagnetic at the DFT

level but magnetic at the PBE + U level, which tends to over-stabilize magnetic solutions. We also note that the material could be carbon deficient, see Sec. S7.18 of the Supplemental Material [45]. For $TaRu_3C$, we show in Figs. 3(k) and 3(l) that only low-energy phonons contribute to the electron-phonon couplings, due to the large phonon density of states at these energies. $TaRu_3C$ also possesses very strong electron-phonon couplings, manifested by $\lambda = 1.77$. The Fermi surface in Fig. 4(f) is composed by a sphere at Γ (invisible in the figure) and connected neck-like formations at R and really small pockets near X. From Fig. 3(i), we note that the Fermi surfaces at the Γ-R and R-X lines, although they have coupled strongly with the phonons, are really sensitive to the shift of Fermi energy. The $T_c^{\mathrm{iso}} = 21.0\,\mathrm{K}$ and $T_c^{\mathrm{aniso}} = 25.0\,\mathrm{K}$ values indicate the somewhat isotropic nature of this material, which is also shown by the homogeneous Cooper-pair density on the Fermi surface in Fig. 4(f). We have shown that these three materials discussed here (and many others identified in this study) host intriguing new physics that is worth further experimental investigation. Even if not presenting a high T_c value, computational approaches might point to new classes of materials to investigate (e.g., half-Heusler) or to materials that could warrant further experimental investigation (e.g., BaB_2).

III. CONCLUSIONS

In conclusion, starting from 4533 experimentally known compounds with 12 atoms or less in the primitive unit cell obtained from the Materials Cloud 3D database and determined to be nonmagnetic metals at the DFT (PBEsol) Kohn-Sham level, we have performed a high-throughput search for novel superconductors using a combination of the QUANTUM ESPRESSO, WANNIER90, and EPW codes. Of the top 250 candidates, 137 have been investigated for superconductivity; for the 82 where we can positively match structures, 74 are also reported as superconductors, giving a 90% ratio of true positives and demonstrating the ability of our approach to flag materials as potential superconductors. Of the remaining 113 that have so far not been reported in the experimental literature, we have 24 with a predicted T_c^{aniso} value above 10 K and we have reported the first bird's eye view of the current state of the art on BCS theory versus experiment in Fig. S4(b) in the Supplemental Material [45]. Among the novel candidates, there is the double-gap superconductor BaB_2, with a predicted T_c value of 61.6 K, the half-Heusler ZrRuSb, with an 11.1 K critical temperature, higher than the 12 known full-Heusler superconductors present in our data set, and the perovskite $TaRu_3C$, with a predicted T_c value of 25.0 K. If experimentally confirmed, ZrRuSb would be the first half-Heusler superconductors with a VEC of 17 to exhibit conventional superconductivity. The present results demonstrate the potential of high-throughput calculations to identify new superconductors and provide a valuable resource for future experimental studies, highlighting not only the predictive power of high-throughput calculations but also their limits. Computationally, this work sets the stage for exploring these databases further, also including larger unit cells, or higher-accuracy Wannierization [52] for electronic band structures, potentially unveiling overlooked superconductors with intriguing physical properties and promising application potential.

IV. METHODS

A. Initial interpolation workflow

Our initial electron-phonon workchain is a workflow that calculates the Eliashberg spectral function based on the linear-interpolation approach of Wierzbowska *et al.* [48]. It consists of the following five steps: (i) a DFT calculation performed on a fine **k**-point, which is used later to perform the linear interpolation; (ii) a second DFT calculation on a coarser grid, required to calculate the phonons in the next step; (iii) a phonon calculation that calculates the electron-phonon coefficients on the coarse **k**-grid with a commensurate **q**-grid; (iv) the calculations of the real-space force constants; and (v) the Fourier interpolation over a dense **q**-grid and to calculate the final electron-phonon coupling and corresponding spectral function on the fine **k**-point grid.

We use pseudopotentials from the Standard Solid-State Pseudopotentials (SSSP) PBEsol efficiency v1.1 [41] library. For each material, we take the highest value for the plane-wave cutoffs among the suggested values for each of the elements present. We use a **k**-point grid that is twice the density of the **q**-grid.

B. EPW interpolation workflow

The EPW pipeline described previously uses several components that run QUANTUM ESPRESSO in combination with EPW to calculate the electron-phonon coupling and the superconducting critical temperature at a high precision (for a schematic representation of the workflow, see Fig. 5). The EPW workchain takes care of the coarse-grid QUANTUM ESPRESSO [47], WANNIER90 [117], and EPW [29,30] calculations that are required for the subsequent interpolations. The workflow consists of the following steps: (i) a first workflow that constructs the Wannier functions for the input structure using the SCDM-k method [32]; (ii) a phonon calculation to compute the dynamical matrices and perturbed potentials; and (iii) the conversion of the input files required for the EPW calculation into the expected format and the running of an EPW calculation on the coarse grid to produce the restart files for the interpolation, which are stashed on the remote machine in a permanent location. For the EPW pipeline, we switch to the norm-conserving PBE pseudopotentials from the scalar-relativistic table

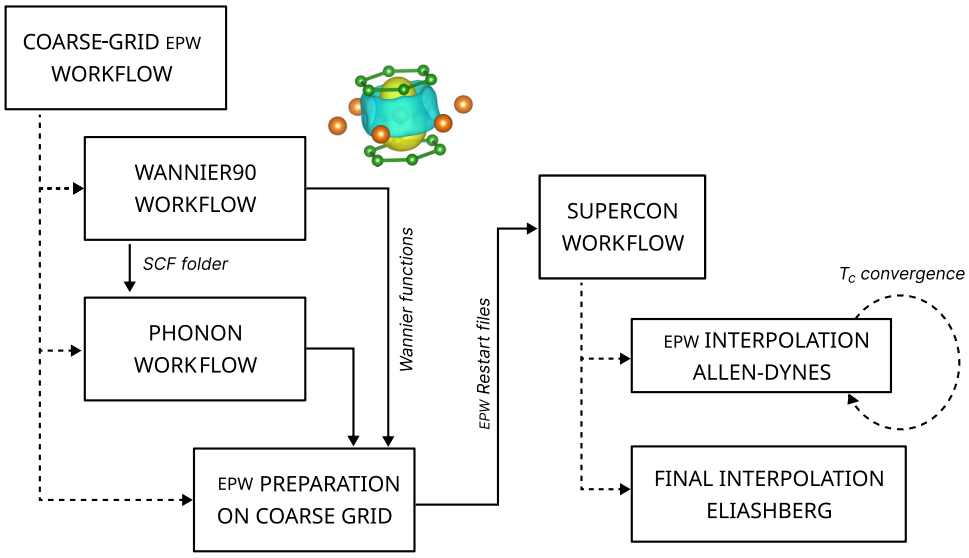

FIG. 5. A schematic of the superconducting workflow, showing the steps executed to obtain the isotropic Eliashberg T_c value using the EPW workflows implemented in AiiDA.

of PseudoDojo v0.5 [43], as projector-augmented-wave-method pseudopotentials have not been extensively tested with the EPW code. For the energy cutoffs, we select the highest hint value for each element and once again take the highest one from the set of atoms contained in each material.

Based on the stashed restart files produced by the first workchain, a second superconducting workchain is run to interpolate the electron-phonon coupling on dense momentum grids and to calculate the superconducting critical temperature. The main feature of this workflow is that it automatically converges the fine-grid interpolation meshes for both the **k**- and **q**-points, based on a calculation of the Allen-Dynes critical temperature and a specified threshold (default 1 K). Once at least three calculations have been performed in the convergence loop and the Allen-Dynes critical temperature has converged, the workflow runs a final calculation on the fine grid using the full Eliashberg theory to calculate the isotropic Eliashberg critical temperature on the converged fine grid.

ACKNOWLEDGMENTS

The authors thank Prof. Miguel Marques for providing feedback on the perovskite $TaRu_3C$. We acknowledge financial support from the NCCR MARVEL, a National Centre of Competence in Research, funded by the Swiss National Science Foundation (Grant No. 205602), as well as the European Centre of Excellence MaX "Materials design at the Exascale" (Grant No. 824143). The work is also supported by a pilot access grant from the Swiss National Supercomputing Centre (CSCS) on the Swiss share of the LUMI system under project ID "PILOT MC EPFL-NM 01," a CHRONOS grant from the CSCS on the Swiss share of the LUMI system under project ID "REGULAR MC EPFL-NM 02," and a grant from the CSCS under project ID mr32. S.P. and Y.Z. acknowledge support from the Fonds de la Recherche Scientifique de Belgique (FRS-FNRS) and T.W011.23 (PDR-WEAVE) and also supported by the Walloon Region in the strategic axe FRFS-WEL-T. M.B. and G.P. gratefully acknowledge support from the SwissT-wins project, funded by the Swiss State Secretariat for Education, Research and Innovation (SERI). G.P. gratefully acknowledges support from the Swiss National Science Foundation (SNSF) Project Funding (Grant No. 200021E_206190 "FISH4DIET"), F.v.R. acknowledges support from SNSF Eccellenza Funding (Grant No. PCEFP2_194183). L.B. and N.M. gratefully acknowledge support from the Deutsche Forschungsgemeinschaft (German Research Foundation, DFG) under Germany's Excellence Strategy (EXC 2077, Grant No. 390741603, University Allowance, University of Bremen) and Lucio Colombi Ciacchi, the host of the "U Bremen Excellence Chair Program". Computational resources have been provided by the Partnership for Advanced Computing in Europe (PRACE) award, granting access to Discoverer in SofiaTech, Bulgaria (OptoSpin project ID: 2020225411), and by the European High Performance Computing Joint Undertaking (EuroHPC JU) award, granting access to MareNostrum5 at Barcelona Supercomputing Center (BSC), Spain (project ID: EHPC-EXT-2023E02-050), and by the Consortium des Équipements de Calcul Intensif (CÉCI), funded by the FRS-FNRS under Grant No. 2.5020.11 and by the Walloon Region, as well as computational resources awarded on the Belgian share of the EuroHPC LUMI supercomputer.

S.P. and N.M. conceived the project, M.B. and S.P. designed the AiiDA workflows, M.B. performed the high-throughput calculations with AiiDA, Y.Z. performed analysis of the stability, sensitivity, and detailed superconductivity, G.T., A.G.G., and M.B performed the literature search, L.B. performed the magnetic calculation with PBE+U+V and the ROMEO code, J.Q. helped with the automatic Wannier function generation, F.v.R. provided experimental guidance, and S.P., G.P., E.C., and N.M. supervised the work. All authors contributed to the writing of the manuscript. These authors contributed equally: Marnik Bercx, Samuel Poncé.

DATA AVAILABILITY

The data that support the findings of this paper are openly available [44].

[1] D. Uglietti, A review of commercial high temperature superconducting materials for large magnets: From wires and tapes to cables and conductors, Supercond. Sci. Technol. **32**, 053001 (2019).

[2] L. Boeri, in *Handbook of Materials Modeling* (Springer International Publishing, Cham, 2018), pp. 1–41.

[3] L. Boeri and G. B. Bachelet, Viewpoint: The road to room-temperature conventional superconductivity, J. Phys.: Condens. Matter **31**, 234002 (2019).

[4] K. M. Shen and J. S. Davis, Cuprate high-T_c superconductors, Mater. Today **11**, 14 (2008).

[5] R. M. Fernandes, A. V. Chubukov, and J. Schmalian, What drives nematic order in iron-based superconductors? Nat. Phys. **10**, 97 (2014).

[6] H. Hosono, K. Tanabe, E. Takayama-Muromachi, H. Kageyama, S. Yamanaka, H. Kumakura, M. Nohara, H. Hiramatsu, and S. Fujitsu, Exploration of new superconductors and functional materials, and fabrication of superconducting tapes and wires of iron pnictides, Sci. Technol. Adv. Mater. **16**, 033503 (2015).

[7] L. Zhang, Y. Wang, J. Lv, and Y. Ma, Materials discovery at high pressures, Nat. Rev. Mater. **2**, 17005 (2017).

[8] S. M. O'Mahony, W. Ren, W. Chen, Y. X. Chong, X. Liu, H. Eisaki, S. Uchida, M. H. Hamidian, and J. C. S. Davis, On the electron pairing mechanism of copper-oxide high temperature superconductivity, Proc. Natl. Acad. Sci. **119**, e2207449119 (2022).

[9] S. Baroni, S. de Gironcoli, A. Dal Corso, and P. Giannozzi, Phonons and related crystal properties from density-functional perturbation theory, Rev. Mod. Phys. **73**, 515 (2001).

[10] F. Giustino, Electron-phonon interactions from first principles, Rev. Mod. Phys. **89**, 019901 (2017).

[11] H. Mori, T. Nomoto, R. Arita, and E. R. Margine, Efficient anisotropic Migdal-Eliashberg calculations with an intermediate representation basis and Wannier interpolation, Phys. Rev. B **110**, 064505 (2024).

[12] A. N. Kolmogorov, S. Shah, E. R. Margine, A. F. Bialon, T. Hammerschmidt, and R. Drautz, New superconducting and semiconducting Fe-B compounds predicted with an *ab initio* evolutionary search, Phys. Rev. Lett. **105**, 217003 (2010).

[13] H. Gou, N. Dubrovinskaia, E. Bykova, A. A. Tsirlin, D. Kasinathan, W. Schnelle, A. Richter, M. Merlini, M. Hanfland, A. M. Abakumov, D. Batuk, G. Van Tendeloo, Y. Nakajima, A. N. Kolmogorov, and L. Dubrovinsky, Discovery of a superhard iron tetraboride superconductor, Phys. Rev. Lett. **111**, 157002 (2013).

[14] V. Stanev, C. Oses, A. G. Kusne, E. Rodriguez, J. Paglione, S. Curtarolo, and I. Takeuchi, Machine learning modeling of superconducting critical temperature, npj Comput. Mater. **4**, 29 (2018).

[15] S. R. Xie, Y. Quan, A. C. Hire, B. Deng, J. M. DeStefano, I. Salinas, U. S. Shah, L. Fanfarillo, J. Lim, J. Kim, G. R. Stewart, J. J. Hamlin, P. J. Hirschfeld, and R. G. Hennig, Machine learning of superconducting critical temperature from Eliashberg theory, npj Comput. Mater. **8**, 14 (2022).

[16] K. Choudhary and K. Garrity, Designing high-T_C superconductors with BCS-inspired screening, density functional theory, and deep-learning, npj Comput. Mater. **8**, 244 (2022).

[17] H. Tran and T. N. Vu, Machine-learning approach for discovery of conventional superconductors, Phys. Rev. Mater. **7**, 054805 (2023).

[18] D. Wines, T. Xie, and K. Choudhary, Inverse design of next-generation superconductors using data-driven deep generative models, J. Phys. Chem. Lett. **14**, 6630 (2023).

[19] E. A. Pogue, A. New, K. McElroy, N. Q. Le, M. J. Pekala, I. McCue, E. Gienger, J. Domenico, E. Hedrick, T. M. McQueen, B. Wilfong, C. D. Piatko, C. R. Ratto, A. Lennon, C. Chung, T. Montalbano, G. Bassen, and C. D. Stiles, Closed-loop superconducting materials discovery, npj Comput. Mater. **9**, 181 (2023).

[20] J. Li, W. Fang, S. Jin, C. Suo, T. Zhang, Y. Wu, X. Xu, Y. Liu, and D.-X. Yao, AI Sci. **1**, 015001 (2025).

[21] X.-Q. Han, Z. Ouyang, P.-J. Guo, H. Sun, Z.-F. Gao, and Z.-Y. Lu, InvDesFlow: An AI-driven materials inverse design workflow to explore possible high-temperature superconductors, Chin. Phys. Lett. **42**, 047301 (2025).

[22] S. Lee, J. Hattrick-Simpers, Y.-J. Kim, and O. A. von Lilienfeld, High-T_c superconductor candidates proposed by machine learning, arXiv:2406.14524 [cond–mat.supr-con].

[23] A. M. Shipley, M. J. Hutcheon, R. J. Needs, and C. J. Pickard, High-throughput discovery of high-temperature conventional superconductors, Phys. Rev. B **104**, 054501 (2021).

[24] T. F. T. Cerqueira, A. Sanna, and M. A. L. Marques, Sampling the materials space for conventional superconducting compounds, Adv. Mater. **36**, 2307085 (2023).

[25] D. Wines, K. Choudhary, A. J. Biacchi, K. F. Garrity, and F. Tavazza, High-throughput DFT-based discovery of next generation two-dimensional (2D) superconductors, Nano Lett. **23**, 969 (2023).

[26] H. Tran, H.-C. Dam, C. Kuenneth, V. Ngoc Tuoc, and H. Kino, Superconductor discovery in the emerging paradigm of materials informatics, Chem. Mater. **36**, 10939 (2024).

[27] T. Sommer, R. Willa, J. Schmalian, and P. Friederich, 3DSC—a dataset of superconductors including crystal structures, Sci. Data **10**, 816 (2023).

[28] E. R. Margine and F. Giustino, Anisotropic Migdal-Eliashberg theory using Wannier functions, Phys. Rev. B **87**, 024505 (2013).

[29] S. Poncé, E. R. Margine, C. Verdi, and F. Giustino, EPW: Electron-phonon coupling, transport and superconducting properties using maximally localized Wannier functions, Comput. Phys. Commun. **209**, 116 (2016).

[30] H. Lee, S. Poncé, K. Bushick, S. Hajinazar, J. Lafuente-Bartolome, J. Leveillee, C. Lian, J.-M. Lihm, F. Macheda, H. Mori, H. Paudyal, W. H. Sio, S. Tiwari, M. Zacharias, X. Zhang, N. Bonini, E. Kioupakis, E. R. Margine, and F. Giustino, Electron-phonon physics from first principles using the EPW code, npj Comput. Mater. **9**, 156 (2023).

[31] N. Marzari, A. A. Mostofi, J. R. Yates, I. Souza, and D. Vanderbilt, Maximally localized Wannier functions: Theory and applications, Rev. Mod. Phys. **84**, 1419 (2012).

[32] A. Damle, L. Lin, and L. Ying, SCDM-k: Localized orbitals for solids via selected columns of the density matrix, J. Comput. Phys. **334**, 1 (2017).

[33] S. P. Huber *et al.*, AiiDA 1.0, a scalable computational infrastructure for automated reproducible workflows and data provenance, Sci. Data **7**, 300 (2020).

[34] M. Uhrin, S. P. Huber, J. Yu, N. Marzari, and G. Pizzi, Workflows in AiiDA: Engineering a high-throughput, event-based engine for robust and modular computational workflows, Comput. Mater. Sci. **187**, 110086 (2021).

[35] Materials Cloud 3D database, available at https://mc3d.materialscloud.org/, accessed: 2024-06-21.

[36] S. Gražulis, A. Daškevič, A. Merkys, D. Chateigner, L. Lutterotti, M. Quirós, N. R. Serebryanaya, P. Moeck, R. T. Downs, and A. Le Bail, Crystallography Open Database (COD): An open-access collection of crystal structures and platform for world-wide collaboration, Nucleic Acids Res. **40**, D420 (2011).

[37] Inorganic Crystal Structure Database (2024).

[38] The Pauling file exposed through the Materials Platform for Data Science, 2024, available at https://mpds.io/.

[39] N. Mounet, M. Gibertini, P. Schwaller, D. Campi, A. Merkys, A. Marrazzo, T. Sohier, I. E. Castelli, A. Cepellotti, G. Pizzi, and N. Marzari, Two-dimensional materials from high-throughput computational exfoliation of experimentally known compounds, Nat. Nanotechnol. **13**, 246 (2018).

[40] A. K. Cheetham and R. Seshadri, Artificial intelligence driving materials discovery? Perspective on the article: Scaling deep learning for materials discovery, Chem. Mater. **36**, 3490 (2024).

[41] G. Prandini, A. Marrazzo, I. E. Castelli, N. Mounet, and N. Marzari, Precision and efficiency in solid-state pseudopotential calculations, npj Comput. Mater. **4**, 72 (2018).

[42] P. E. Blöchl, Projector augmented-wave method, Phys. Rev. B **50**, 17953 (1994).

[43] M. van Setten, M. Giantomassi, E. Bousquet, M. Verstraete, D. Hamann, X. Gonze, and G.-M. Rignanese, The PseudoDojo: Training and grading a 85 element optimized norm-conserving pseudopotential table, Comput. Phys. Commun. **226**, 39 (2018).

[44] Materials Cloud archive, 2025, available at https://archive.materialscloud.org/record/2025.39, accessed: 2025-03-13.

[45] See the Supplemental Material at http://link.aps.org/supplemental/10.1103/sb28-fjc9 for more details about the MC3D database of materials, convergence with momentum grids and workflow error rate, comparison with experiment, Hubbard calculations, sensitivity analysis of the superconducting prediction, detailed analysis for BaB_2, and full EPW pipeline results.

[46] P. B. Allen and R. C. Dynes, Transition temperature of strong-coupled superconductors reanalyzed, Phys. Rev. B **12**, 905 (1975).

[47] P. Giannozzi *et al.*, Advanced capabilities for materials modelling with QUANTUM ESPRESSO, J. Phys.: Condens. Matter **29**, 465901 (2017).

[48] M. Wierzbowska, S. de Gironcoli, and P. Giannozzi, Origins of low- and high-pressure discontinuities of T_c in niobium, arXiv:cond-mat/0504077 [cond-mat.supr-con].

[49] I. M. Eremin, J. Knolle, and R. Moessner, in *Handbook of Magnetism and Magnetic Materials* (Springer International Publishing, Cham, 2020), pp. 1–31.

[50] C. Lin, S. Poncé, and N. Marzari, General invariance and equilibrium conditions for lattice dynamics in 1D, 2D, and 3D materials, npj Comput. Mater. **8**, 236 (2022).

[51] X. Gonze and C. Lee, Dynamical matrices, born effective charges, dielectric permittivity tensors, and interatomic force constants from density-functional perturbation theory, Phys. Rev. B **55**, 10355 (1997).

[52] J. Qiao, G. Pizzi, and N. Marzari, Projectability disentanglement for accurate and automated electronic-structure Hamiltonians, npj Comput. Mater. **9**, 208 (2023).

[53] Y. M. Shy, L. E. Toth, and R. Somasundaram, Superconducting properties, electrical resistivities, and structure of NbN thin films, J. Appl. Phys. **44**, 5539 (1973).

[54] K. R. Babu and G.-Y. Guo, Electron-phonon coupling, superconductivity, and nontrivial band topology in NbN polytypes, Phys. Rev. B **99**, 104508 (2019).

[55] M. Kawamura, Y. Hizume, and T. Ozaki, Benchmark of density functional theory for superconductors in elemental materials, Phys. Rev. B **101**, 134511 (2020).

[56] L. Reining, The *GW* approximation: Content, successes and limitations, WIREs Comput. Mol. Sci. **8**, e1344 (2017).

[57] J. Nagamatsu, N. Nakagawa, T. Muranaka, Y. Zenitani, and J. Akimitsu, Superconductivity at 39 K in magnesium diboride, Nature **410**, 63 (2001).

[58] A. Y. Ganin, L. Kienle, and G. V. Vajenine, Synthesis and characterisation of hexagonal molybdenum nitrides, J. Solid State Chem. **179**, 2339 (2006).

[59] G. Stewart, Superconductivity in the A15 structure, Physica C: Supercond. Appl. **514**, 28 (2015).

[60] X. Xu, A review and prospects for Nb_3Sn superconductor development, Supercond. Sci. Technol. **30**, 093001 (2017).

[61] J. J. Lin, S. M. Huang, Y. H. Lin, T. C. Lee, H. Liu, X. X. Zhang, R. S. Chen, and Y. S. Huang, Low temperature electrical transport properties of RuO_2 and IrO_2 single crystals, J. Phys.: Condens. Matter **16**, 8035 (2004).

[62] T. Skośkiewicz, Superconductivity in the palladium-hydrogen system, Phys. Status Solidi (b) **59**, 329 (1973).

[63] J. Harper, Effect of hydrogen concentration on superconductivity and clustering in palladium hydride, Phys. Lett. A **47**, 69 (1974).

[64] M. Van Maaren and G. Schaeffer, Some new superconducting group Va dichalcogenides, Phys. Lett. A **24**, 645 (1967).

[65] I. Guillamón, H. Suderow, S. Vieira, L. Cario, P. Diener, and P. Rodière, Superconducting density of states and vortex cores of 2H-NbS_2, Phys. Rev. Lett. **101**, 166407 (2008).

[66] J. Eisenstein, Superconducting elements, Rev. Mod. Phys. **26**, 277 (1954).

[67] J. Hamlin, Superconductivity in the metallic elements at high pressures, Physica C: Supercond. Appl. **514**, 59 (2015).

[68] L. Toth and J. Zbasnik, Low temperature heat capacities of superconducting molybdenum carbides, Acta Metall. **16**, 1177 (1968).

[69] S. Ramakrishnan, A. K. Nigam, and G. Chandra, Resistivity and magnetoresistance studies on superconducting A15 V_3Ga, V_3Au, and V_3Pt compounds, Phys. Rev. B **34**, 6166 (1986).

[70] W. T. Ziegler and R. A. Young, Studies of compounds for superconductivity, Phys. Rev. **90**, 115 (1953).

[71] C. Witteveen, K. Górnicka, J. Chang, M. Månsson, T. Klimczuk, and F. O. von Rohr, Polytypism and superconductivity in the NbS_2 system, Dalton Trans. **50**, 3216 (2021).

[72] D. W. Murphy, F. J. Di Salvo, G. W. Hull, J. V. Waszczak, S. F. Meyer, G. R. Stewart, S. Early, J. V. Acrivos, and T. H. Geballe, Properties of H_xTaS_2: Correlation between the superconducting T_c and an electronic instability in layer compounds, J. Chem. Phys. **62**, 967 (1975).

[73] E. Navarro-Moratalla, J. O. Island, S. Mañas-Valero, E. Pinilla-Cienfuegos, A. Castellanos-Gomez, J. Quereda, G. Rubio-Bollinger, L. Chirolli, J. A. Silva-Guillén, N. Agraït, G. A. Steele, F. Guinea, H. S. J. van der Zant, and E. Coronado, Enhanced superconductivity in atomically thin TaS_2, Nat. Commun. **7**, 11043 (2016).

[74] H. Rosner, W. E. Pickett, S.-L. Drechsler, A. Handstein, G. Behr, G. Fuchs, K. Nenkov, K.-H. Müller, and H. Eschrig, Electronic structure and weak electron-phonon coupling in TaB_2, Phys. Rev. B **64**, 144516 (2001).

[75] T. H. Courtney, G. W. Pearsall, and J. Wulff, Effect of processing history on the superconducting properties and long-range order of Ta_3Sn, J. Appl. Phys. **36**, 3256 (1965).

[76] S. Wada and K. Asayama, Nuclear quadrupole spin-lattice relaxation of Ta^{181} in type II superconducting Ta_3Sn, J. Phys. Soc. Jpn. **34**, 1168 (1973).

[77] R. L. Cappelletti, D. M. Ginsberg, and J. K. Hulm, Far-infrared absorption in superconducting niobium alloys, Phys. Rev. **158**, 340 (1967).

[78] B. T. Matthias, T. H. Geballe, and V. B. Compton, Superconductivity, Rev. Mod. Phys. **35**, 1 (1963).

[79] B. T. Matthias, Empirical relation between superconductivity and the number of valence electrons per atom, Phys. Rev. **97**, 74 (1955).

[80] R. Flukiger, A. Paoli, and J. Muller, Electronically "atypical" A15-type compounds based on chromium and molybdenum, Solid State Commun. **14**, 443 (1974).

[81] N. Emery, C. Hérold, M. d'Astuto, V. Garcia, C. Bellin, J. F. Marêché, P. Lagrange, and G. Loupias, Superconductivity of bulk CaC, Phys. Rev. Lett. **95**, 087003 (2005).

[82] G. F. Hardy and J. K. Hulm, The superconductivity of some transition metal compounds, Phys. Rev. **93**, 1004 (1954).

[83] R. Müller, R. Shelton, J. Richardson, and R. Jacobson, Superconductivity and crystal structure of a new class of ternary transition metal phosphides TT/t'P (TZr, Nb, Ta and T/t'Ru, Rh), J. Less Common Met. **92**, 177 (1983).

[84] A. Simon, M. Bäcker, R. W. Henn, C. Felser, R. K. Kremer, H. Mattausch, and A. Yoshiasa, Supraleitung in Seltenerdmetall-Carbidhalogeniden des Typs $SE_2X_2C_2$, Z. Anorg. Allg. Chem. **622**, 123 (1996).

[85] M. Uehara, A. Uehara, K. Kozawa, T. Yamazaki, and Y. Kimishima, New antiperovskite superconductor $ZnNNi_3$, and related compounds $CdNNi_3$ and $InNNi_3$, Physica C: Supercond. Appl. **470**, S688 (2010).

[86] A. Giorgi and E. Szklarz, Superconductivity of technetium and technetium carbide, J. Less Common Met. **11**, 455 (1966).

[87] J. Hulm, M. Walker, and N. Pessall, High T_c-experimental achievement, Physica **55**, 60 (1971).

[88] R. J. Xiao, K. Q. Li, H. X. Yang, G. C. Che, H. R. Zhang, C. Ma, Z. X. Zhao, and J. Q. Li, Correlations among superconductivity, structural instability, and band filling in $Nb_{1-x}B_2$ at the critical point $x \approx 0.2$, Phys. Rev. B **73**, 224516 (2006).

[89] M. Mudgel, V. Awana, G. Bhalla, and H. Kishan, Superconductivity of non-stoichiometric intermetallic compound NbB_2, Solid State Commun. **147**, 439 (2008).

[90] R. Potjan, M. Wislicenus, O. Ostien, R. Hoffmann, M. Lederer, A. Reck, J. Emara, L. Roy, B. Lilienthal-Uhlig, and J. Wosnitza, 300 mm CMOS-compatible superconducting HfN and ZrN thin films for quantum applications, Appl. Phys. Lett. **123**, 172602 (2023).

[91] H. Fukuoka, Y. Tomomitsu, and K. Inumaru, High-pressure synthesis and superconductivity of a new binary barium germanide $BaGe_3$, Inorg. Chem. **50**, 6372 (2011).

[92] R. Castillo, A. I. Baranov, U. Burkhardt, R. Cardoso-Gil, W. Schnelle, M. Bobnar, and U. Schwarz, Germanium dumbbells in a new superconducting modification of $BaGe_3$, Inorg. Chem. **55**, 4498 (2016).

[93] A. R. Moodenbaugh, D. C. Johnston, R. Viswanathan, R. N. Shelton, L. E. DeLong, and W. A. Fertig, Superconductivity of transition metal sulfides, selenides, and phosphides with the NaCl structure, J. Low Temp. Phys. **33**, 175 (1978).

[94] D. Campi, S. Kumari, and N. Marzari, Prediction of phonon-mediated superconductivity with high critical temperature in the two-dimensional topological semimetal W_2N_3, Nano Lett. **21**, 3435 (2021).

[95] S. Chen, Z. Wu, Z. Zhang, S. Wu, K.-M. Ho, V. Antropov, and Y. Sun, High-throughput screening for boride superconductors, Inorg. Chem. **63**, 8654 (2024).

[96] I. Timrov, N. Marzari, and M. Cococcioni, Self-consistent Hubbard parameters from density-functional perturbation theory in the ultrasoft and projector-augmented wave formulations, Phys. Rev. B **103**, 045141 (2021).

[97] I. Timrov, N. Marzari, and M. Cococcioni, HP—a code for the calculation of Hubbard parameters using density-functional perturbation theory, Comput. Phys. Commun. **279**, 108455 (2022).

[98] L. Bastonero *et al.*, First-principles hubbard parameters with automated and reproducible workflows, npj Comput. Mater. **11**, 183 (2025).

[99] H. J. Kulik, M. Cococcioni, D. A. Scherlis, and N. Marzari, Density functional theory in transition-metal chemistry: A self-consistent Hubbard *U* approach, Phys. Rev. Lett. **97**, 103001 (2006).

[100] N. Marzari, A. Ferretti, and C. Wolverton, Electronic-structure methods for materials design, Nat. Mater. **20**, 736 (2021).

[101] A. DePalma, Fast H^+-ion implantation enables precise Fermi level engineering in quantum materials, MRS Bull. **49**, 1189 (2024).

[102] J. A. Grovogui, T. J. Slade, S. Hao, C. Wolverton, M. G. Kanatzidis, and V. P. Dravid, Implications of doping on microstructure, processing, and thermoelectric performance: The case of PbSe, J. Mater. Res. **36**, 1272 (2021).

[103] C. B. Evers, C. G. Richter, K. Hartjes, and W. Jeitschko, Ternary transition metal antimonides and bismuthides with MgAgAs-type and filled NiAs-type structure, J. Alloys Compd. **252**, 93 (1997).

[104] J. Winterlik, G. H. Fecher, C. Felser, M. Jourdan, K. Grube, F. Hardy, H. von Löhneysen, K. L. Holman, and R. J. Cava, Ni-based superconductor: Heusler compound $ZiNi_2Ga$, Phys. Rev. B **78**, 184506 (2008).

[105] S. Anand, K. Xia, V. I. Hegde, U. Aydemir, V. Kocevski, T. Zhu, C. Wolverton, and G. J. Snyder, A valence balanced rule for discovery of 18-electron half-Heuslers with defects, Energy Environ. Sci. **11**, 1480 (2018).

[106] T. Graf, C. Felser, and S. S. Parkin, Simple rules for the understanding of Heusler compounds, Prog. Solid State Chem. **39**, 1 (2011).

[107] N. Hoffmann, T. F. T. Cerqueira, P. Borlido, A. Sanna, J. Schmidt, and M. A. L. Marques, Searching for ductile superconducting Heusler X_2YZ compounds, npj Comput. Mater. **9**, 138 (2023).

[108] C. Timm, A. P. Schnyder, D. F. Agterberg, and P. M. R. Brydon, Inflated nodes and surface states in superconducting half-Heusler compounds, Phys. Rev. B **96**, 094526 (2017).

[109] H. Xiao, T. Hu, W. Liu, Y. L. Zhu, P. G. Li, G. Mu, J. Su, K. Li, and Z. Q. Mao, Superconductivity in the half-Heusler compound TbPdBi, Phys. Rev. B **97**, 224511 (2018).

[110] F. F. Tafti, T. Fujii, A. Juneau-Fecteau, S. René de Cotret, N. Doiron-Leyraud, A. Asamitsu, and L. Taillefer, Superconductivity in the noncentrosymmetric half-Heusler compound LuPtBi: A candidate for topological superconductivity, Phys. Rev. B **87**, 184504 (2013).

[111] M. Smidman, M. B. Salamon, H. Q. Yuan, and D. F. Agterberg, Superconductivity and spin-orbit coupling in non-centrosymmetric materials: A review, Rep. Prog. Phys. **80**, 036501 (2017).

[112] M. Kim, G. M. McNally, H.-H. Kim, M. Oudah, A. S. Gibbs, P. Manuel, R. J. Green, R. Sutarto, T. Takayama, A. Yaresko, U. Wedig, M. Isobe, R. K. Kremer, D. A. Bonn, B. Keimer, and H. Takagi, Superconductivity in $(Ba, K)SbO_3$, Nat. Mater. **21**, 627 (2022).

[113] N. Hoffmann, T. F. T. Cerqueira, J. Schmidt, and M. A. L. Marques, Superconductivity in antiperovskites, npj Comput. Mater. **8**, 150 (2022).

[114] C. P. Poole, *Handbook of Superconductivity* (Elsevier, Amsterdam, 2000).

[115] E. Emetere Moses, Microstructural and electronics dynamics of barium diboride as a superconductor from first principles, Results Phys. **19**, 103658 (2020).

[116] L. Ponet, E. Di Lucente, and N. Marzari, The energy landscape of magnetic materials, npj Comput. Mater. **10**, 151 (2024).

[117] G. Pizzi *et al.*, WANNIER90 as a community code: New features and applications, J. Phys.: Condens. Matter **32**, 165902 (2020).